Full 3D CFD and FEM Validation of Surrogate-Optimized Hydraulic Manifolds Designed via the MOThEA Framework

Samuele Nizzardo[1], **Andrea Vacca**[2], **Alberto Benato**[1]

[1]*Department of Industrial Engineering, University of Padova, Via Venezia 1, Padova, 35131, Italy, Europe, samuele.nizzardo@phd.unipd.it, alberto.benato@unipd.it*
[2]*Maha Fluid Power Research Center, Purdue University, 1500 Kepner Dr, Lafayette, 47905-6578, IN, USA, avacca@purdue.edu*

Abstract

Despite their high power density and robust performance in aerospace and mobile applications, traditional hydraulic actuation systems are increasingly scrutinized for their energy consumption and operational efficiency. In this context, optimization of the hydraulic manifold architecture plays a key role. The internal routing of these components strongly affects both steady-state flow losses and overall structural mass, making manifold layout a critical factor in improving fluid-dynamic performance and the efficiency of next-generation hydraulic systems.
This paper presents the CFD and structural validation of a fully automated design algorithm for the generation of optimized internal flow topologies in additively manufactured hydraulic manifolds (MOThEA, Manifold design Optimization through Theta* path finder and Evolutionary Algorithms). The proposed framework implements a self-executing sizing methodology that estimates pressure drops using an adapted Ito correlation and determines the minimum safe wall thickness through Lamé equations. Compared with conventional design workflows, which typically require time-consuming manual iterations, the proposed approach significantly reduces design time (less than 25 minutes for a complex real-world application) while enabling a systematic exploration of highly efficient manifold configurations. To validate the algorithm, a reference optimized manifold geometry was analyzed. Assuming the same material, the CFD results show that the optimized topology reduces pressure losses by more than 84% compared to a conventional cross-drilled baseline. At the same time, finite element structural analysis shows that despite a 93.1% reduction in weight, the optimized manifold satisfies structural integrity requirements under operating pressure. Although the present mass evaluation does not include valve-thread connections or support structures, the results demonstrate the reliability of the proposed algorithm in generating feasible ultra-lightweight manifolds with markedly reduced parasitic losses.

Keywords: Computational Fluid Dynamics, Finite Element Method, Manifold Optimization, MOThEA, 3D Routing Planning, Mass Reduction, Pressure Losses Reduction.

1. INTRODUCTION

Hydraulic actuation systems are a fundamental component of modern aerospace vehicles, where efficiency, reliability, weight, and integration constraints play a critical role in overall system performance. Within these systems, hydraulic manifolds significantly influence both energy efficiency and structural weight, as internal pressure losses and material distribution directly affect power off-take requirements and integration margins. In this context, there is significant ongoing research focused on enhancing the efficiency of hydraulic systems (HSs), and the following are just a few examples of the entire landscape. Beltrami et al. [1] investigated the electrification of compact off-highway vehicles, Mahato and Ghoshal [2] reviewed energy-saving strategies in hydraulic power systems, Quan et al. [3] surveyed powertrain technologies for energy-efficient heavy-duty machinery, Li et al. [4] reviewed flow-matching technologies for hydraulic systems, Du et al. [5] presented a comprehensive review of high-efficiency electro-hydrostatic actuator technologies with energy recovery, and Padovani et al. [6] discussed the challenges and possible solutions for designing energy-efficient and low-pollutant machines in off-road hydraulics.

Fundamentally, the main aim of a manifold is to direct the hydraulic fluid in the desired direction with the right pressure, increasing the compactness of the system, supporting valves and probes. From an industrial perspective, pressure losses (PLs) within manifolds are primarily attributed to valves because they reduce the available flow area and increase localized pressure losses (LPLs). However, even though this mechanism is partly unavoidable, the design of the manifold itself strongly affects hydraulic performance, as well as its weight.

In recent years, the scientific community has started considering manifold optimization (MO) as an important research direction. In particular, MO is focusing on the design optimization of already existing manifolds, exploiting computational fluid dynamics (CFD) and additive manufacturing (AM) machining. For example, Abe et al. [7] studied the pressure drops associated with two different manifold block machining strategies by combining CFD analysis and experimental tests, while Zhang et al. [8] used a genetic algorithm to define the connection order of a network. Alshare et al. [9] investigated the feasibility of AM for the production of efficient valve manifolds for hydraulic actuators by redesigning conventionally manufactured valve blocks. Hong et al. [10] developed a method for flow-channel optimization based on 3D printing.

A first attempt to move toward a more generalized design methodology was proposed by Zhu et al. [11], who developed a design approach of hydraulic manifolds using Selective Laser Melting with a particular focus on fluid flow to reduce both pressure losses and manifold weight. Similarly, Rolinck et al. [12] introduced a development methodology for hydraulic manifolds and fluid components manufactured by laser powder bed fusion. Their process systematically leads to parts with improved performance, economic efficiency, and manufacturability. Again, Zhang et al. [13] developed a multi-objective layout design approach for lightweight and energy-saving hydraulic manifolds, and lastly, Zhang et al. [14] refined their design approach moving to an A*–based algorithm to increase the flexibility of the previous proposed method, moving to the automation of the process. The last two studies represent important steps toward more automated design procedures and, while the first is closely tied to specific manifold configurations, the second provides a more general approach.

To further push the boundaries of automated design, the authors recently developed MOThEA (Manifold design optimization through Theta* path finder and Evolutionary Algorithms), a fully automated and general design framework for the synthesis of hydraulic manifolds. MOThEA establishes a computer-aided design (CAD) methodology for 3D geometry synthesis, generating internal paths aimed at reducing both global pressure losses and structural mass. To drastically reduce computational costs during the evolutionary loop, MOThEA relies on fast analytical surrogate models: the analytical integration of Ito's equation along the 3D splines for fluid pressure drops, and Lamé's theory of thick-walled cylinders for structural thickness sizing. While these 1D/2D analytical surrogates enable the evaluation of thousands of individuals in an acceptable time-frame, they inherently simplify complex 3D phenomena, such as fully developed Dean vortices, flow

separations at junctions, and realistic 3D von Mises stress concentrations under high-pressure loads. Therefore, the present work proposes a rigorous computational validation via full 3D CFD and FEM analyses of the optimized manifolds generated by the MOThEA framework. The primary goal of this study is to assess the accuracy of the surrogate models and validate the proposed optimized designs from both a fluid dynamic and structural integrity perspective. Full-scale 3D numerical simulations are employed to verify that the analytical assumptions do not compromise the actual physics of the manifold under real operating conditions.
To highly emphasize the improvements brought by the optimization, a reference baseline configuration (an unoptimized, straightforward orthogonal geometry) is also cross-evaluated and compared. At the end of the proposed design approach, the only structural details omitted from the simulations are the valve-thread connections and external customized mounting supports.
The remainder of the paper is organized as follows. Section 2 briefly introduces the analytical models implemented in MOThEA. Section 3 presents the numerical set-up of the analyses for both CFD and FEM evaluations. Section 4 discusses the fluid-structural comparison between the baseline and the optimized geometries. Finally, Section 5 summarizes the main findings and outlines future developments.

2. ANALYTICAL SURROGATE MODELS

To contextualize the subsequent 3D numerical validation, it is necessary to briefly outline both the MOThEA framework and the analytical surrogate models it employs during the optimization loop.
MOThEA couples three stages into a single automated pipeline. First, a Theta* path finder (PF) builds, within the discretized design domain, an initial collision-free routing between the prescribed ports, which is subsequently discretized into a set of guide-points. Theta* PF denotes the any-angle path-planning algorithm used to generate the initial routing: like the classical A* search, it expands the nodes of a weighted graph to minimize a cost function $f(n) = g(n) + h(n)$, where $g(n)$ is the accumulated path cost from the start node and $h(n)$ an admissible Euclidean heuristic to the goal. However, unlike A*, it allows a node's parent to be any node in line of sight rather than only an adjacent grid neighbour, producing shorter and smoother routes that are not constrained to the grid directions. Second, a hybrid stochastic multi-objective optimizer refines this routing in continuous space: the design variables are the guide-point coordinates and the channel internal diameters d_{in} (port locations may also be released as variables when not fixed a priori), while the two competing objectives are the manifold mass and the aggregate pressure drop, both evaluated through the analytical surrogates described below. The search combines Success-History Adaptive Differential Evolution (SHADE) and Population-Based Incremental Learning with Adaptive Learning Rate (PBIL-ALR) with a semi-dynamic elitism operator. Geometric feasibility (minimum inter-branch clearance, obstacle avoidance, near-orthogonal attachment at the external ports, and non-coincidence of successive control points) is enforced through an ε-relaxed variant of Deb's feasibility rules. Third, the converged spline centrelines and diameters are swept into a software-independent solid model ready for AM. The full formulation of the optimizer is detailed in the companion MOThEA design study.
To avoid computationally expensive 3D simulations during evolutionary generation, the algorithm synthesizes the manifold topology relying on Lamé's formulation for structural sizing and Ito's correlation for fluid dynamic losses along 3D spline paths.

2.1. Structural Mass Evaluation

Because standard thin-walled approximations are inadequate for high-pressure hydraulic components, the minimum required wall thickness (t_{min}) for each generated channel is sized according to Lamé's thick-walled cylinder theory. The structural constraints are analytically embedded using a predefined safety factor (SF):

$$t_{\min} = \frac{d_{\text{in}}}{2}\left(\sqrt{\frac{\sigma_{\text{al}} + p_{\max}}{\sigma_{\text{al}} - p_{\max}}} - 1\right) \tag{2.1}$$

where d_{in} is the diameter of the internal channel, $\sigma_{\text{al}} = \sigma_{\text{y}}/SF$ is the allowable material yield stress, and $p_{\max}$ is the maximum operating pressure. The wall material of a channel of length L forms an annulus of cross-sectional area $\frac{\pi}{4}(d_{\text{out}}^2 - d_{\text{in}}^2)$, with outer diameter $d_{\text{out}} = d_{\text{in}} + 2t_{\min}$. Substituting the thickness from the previous equation gives $d_{\text{out}} = d_{\text{in}}\sqrt{(\sigma_{\text{al}} + p_{\max})/(\sigma_{\text{al}} - p_{\max})}$, so that

$$d_{\text{out}}^2 - d_{\text{in}}^2 = d_{\text{in}}^2\left[\frac{\sigma_{\text{al}} + p_{\max}}{\sigma_{\text{al}} - p_{\max}} - 1\right] = d_{\text{in}}^2\,\frac{2\,p_{\max}}{\sigma_{\text{al}} - p_{\max}}.$$

Collecting this pressure- and material-dependent factor into a global load constant K,

$$K = \frac{2\,p_{\max}}{\sigma_{\text{al}} - p_{\max}} = \frac{2}{\dfrac{\sigma_{\text{al}}}{p_{\max}} - 1}, \tag{2.2}$$

the theoretical printable mass of the topological structure is thereby computed as:

$$m_a = \frac{\pi}{4}\,K\,\rho_{\text{s}}\,d_{\text{in}}^2\,L \tag{2.3}$$

where ρ_{s} is the density of the AM alloy and L is the true geometric arc length of the channel. Note that the structural mass scales with the geometric length L (the physical amount of material), whereas the curvature-enhanced effective length L_{eff} introduced in Section 2.2 enters only the fluid-resistance model.

2.2. Pressure Losses Estimation

Rather than applying discrete lumped loss coefficients to macroscopic bends, MOThEA analytically predicts the pressure drop by treating curvature-induced secondary flows (e.g. Dean vortices) as an equivalent distributed friction. This is achieved by continuously integrating Ito's relation [15] along the curvilinear abscissa s. The resulting effective length L_{eff} serves as the straight-pipe thermodynamic equivalent of the complex 3D non-planar spline:

$$L_{\text{eff}} = \int_0^L \left[1 + 0.14\left(\frac{d_{\text{in}}}{2R(s)}\right)^{0.97}\right] ds \tag{2.4}$$

where $R(s)$ is the local analytical radius of curvature and L is the true geometric arc length.
The distributed pressure drop Δp_{d} is then calculated using a parameterized Darcy-Weisbach formulation for a target volumetric flow rate Q:

$$\Delta p_{\text{d}} = \frac{8\,\rho_f\,f_{\text{t}}}{\pi^2\,d_{\text{in}}^5}\,Q^2\,L_{\text{eff}} \tag{2.5}$$

where ρ_f is the density of the working fluid. The parameter f_{t} is the turbulent friction factor, explicitly evaluated via the Swamee-Jain equation [16] and bounded by the local Reynolds number and the typical relative AM surface roughness (Ra/d_{in}). The fully-turbulent assumption is justified by the maximum-flow boundary conditions.
Finally, purely localized losses (Δp_{l}) are restricted exclusively to macroscopic fluid-domain transitions—namely, sudden contractions at the inlets (C_{in}) and sudden expansions at the outlets (C_{out}):

$$\Delta p_{\text{l}} = \frac{8\,\rho_f}{\pi^2\,d_{\text{in}}^4}\,Q^2\sum_{i=1}^{k}(C_{\text{in}} + C_{\text{out}})_i \tag{2.6}$$

with k being the total number of independent manifold channels.

3. NUMERICAL SET-UP

The geometry of the manifold before optimization is depicted in Figure 3.1b. It is a conventional 5-axis drilled manifold composed of two main blocks: the pre-filter section and the post-filter section. Figure 3.1a highlights the internal flow domain. The optimized geometries generated via MOThEA are shown in Figure 3.2, where

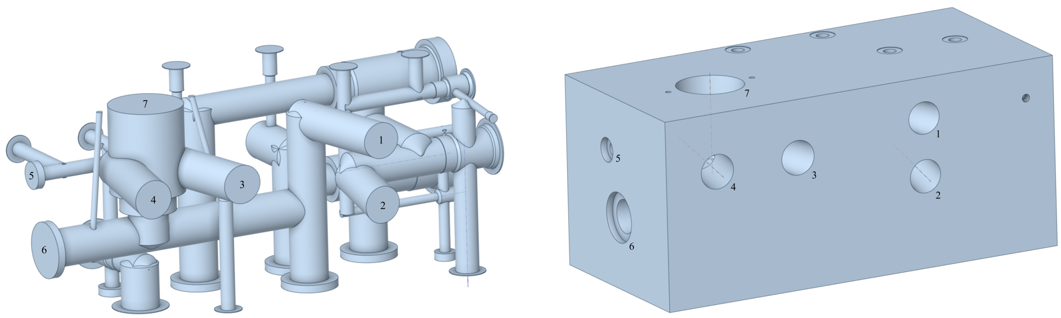

(a) (b)

Figure 3.1. *Reference manifold from a real-world hydraulic application in a coil compactor machine. (a) Internal topology of the conventionally manufactured manifold; (b) corresponding external shape. Equal numbering denotes corresponding boundary ports.*

Figure 3.2a and Figure 3.2b represent the pre-filter and the post-filter blocks respectively, while Figure 3.2c displays the assembled solution. Note that port "6" of the baseline is a drilling-process access hole with no functional flow role; its omission from the synthesized layout therefore leaves the hydraulic function of the manifold unchanged.

3.1. CFD Validation Framework

Computational Fluid Dynamics enables the detailed evaluation of flow fields across complex spatial geometries without requiring physical prototyping. This study utilizes steady-state Reynolds-Averaged Navier-Stokes (RANS) equations to provide a reliable and validated balance between computational efficiency and physical accuracy. The commercial suite ANSYS Fluent was adopted to perform fluid dynamic validation. For a steady-state framework (excluding the initial transient filling phase), the conservative governing equations for continuity, momentum, and energy are formulated as follows:

$$\frac{\partial(\rho u_j)}{\partial x_j} = 0 \tag{3.1}$$

$$\frac{\partial(\rho u_i u_j)}{\partial x_j} = -\frac{\partial p}{\partial x_i} + \frac{\partial \tau_{ij}}{\partial x_j} \tag{3.2}$$

$$\frac{\partial(\rho e u_j + p u_j)}{\partial x_j} = -\frac{\partial q_j}{\partial x_j} + \frac{\partial(\tau_{ij} u_i)}{\partial x_j} \tag{3.3}$$

where $\rho = \rho_f$ is the fluid density (subscript "f" was avoided for clarity of the equations), x_j specifies the Cartesian coordinate direction (with $j = 1,2,3$), u_j is the mean velocity component, p is the static pressure, τ_{ij} represents the effective fluid stress tensor (incorporating both molecular viscosity and turbulent Reynolds stresses), e is the total specific energy, and q_j is the heat flux.
The turbulence closure was achieved using the two-equation $k-\omega$ *SST* model, enhanced with *Low-Reynolds* number corrections, as the maximum expected Reynolds number typically lies within the transitional to fully turbulent boundary ($Re_{\max} \leq 6.5 \times 10^4$).

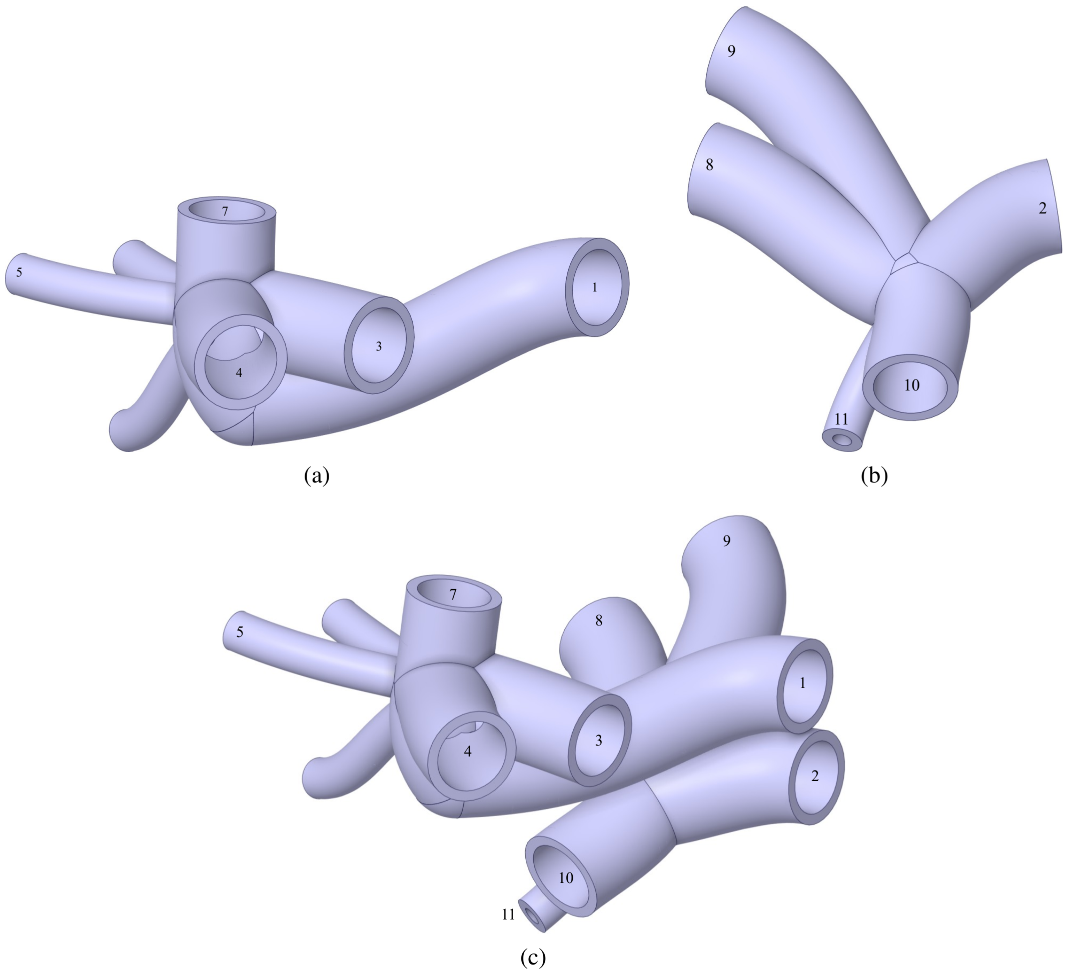

Figure 3.2. *Optimized manifold geometry. Figure (a) is the pre-filter block, while Figure (b) represents the post-filter side. Figure (c) exposes a viable embedded solution between the two blocks. Numbered ports directly map to the conventional baseline references in Figure 3.1. In particular, ports "1", "3", and "4" represent the inlet and distribution outlets of the post-filter block. Ports "2", "8", and "9" act as the outlet and inlets of the pre-filter block, whereas ports "10" and "11" identify static probing/valve lines. Ports "5" and "7" correspond to probe lines. Port "6" of the baseline is a drilling-process access hole with no functional flow role; it is therefore absent from the synthesized layout, which leaves the hydraulic function of the manifold unchanged.*

To ensure grid independence, three different unstructured tetrahedral grids were evaluated for both the pre- and post-filter fluid domains: coarse ($\sim 0.8 \times 10^6$ elements), medium ($\sim 2.3 \times 10^6$ elements), and fine ($\sim 6.2 \times 10^6$ elements). The medium density meshes were ultimately selected, as they yielded asymptotic invariants compared to the fine grid, thus optimizing the computational cost. To properly resolve the momentum and thermal boundary layers, guaranteeing a non-dimensional wall distance $y^+ \leq 1$, a wall-normal inflation layer composed of structured prismatic elements was strictly enforced on all no-slip boundaries. Figure 3.3 illustrates the medium-sized computational grid for the post-filter block (Figure 3.3a) alongside a detailed view of the inflation layers (Figure 3.3b). For the sake of conciseness, the pre-filter mesh highlights are omitted.

The imposed boundary conditions reflect the nominal operational state of the hydraulic circuit, using *Velocity*

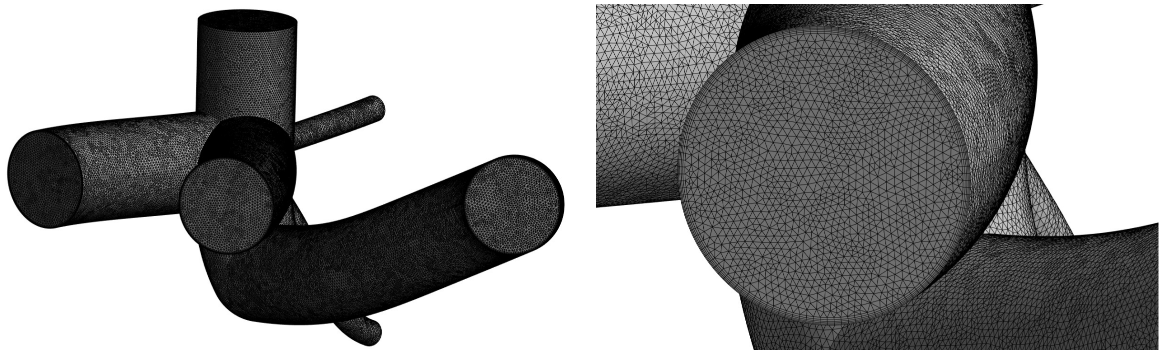

(a) (b)

Figure 3.3. *Representation of the unstructured computational mesh. (a) Post-filter fluid domain volume grid; (b) detailed cut-plane highlighting the near-wall prism layer inflation.*

Inlet and *Pressure Outlet* formulations. The two blocks are analyzed as separate fluid domains, following the port mapping of Figure 3.2. In the pre-filter domain, a velocity inlet is prescribed at each of the two feed ports “8” and “9”, and a pressure outlet at port “2”; in the post-filter domain, a velocity inlet is prescribed at port “1” and pressure outlets at the two distribution ports “3” and “4”. The static probing/valve lines (ports “10” and “11”) carry no net flow and are treated as no-slip walls. The prescribed inlet velocities correspond to a nominal volumetric flow rate of $Q = 400$ L/min ($200 + 200$ L/min at ports "8" and "9"), while the static pressure at the outlets is set to 140 bar. The same inlet flow rates and the same inlet split were imposed on the baseline and the optimized geometries, so that the two configurations are compared under strictly identical boundary conditions. To simulate the friction induced by conventional and additive manufacturing, an equivalent sand-grain roughness of $H_{\text{Ra}} = 5 \times 10^{-5}$ m was assigned to the wall boundaries. The thermal gradients were modeled by imposing a uniform wall temperature $T_{\text{w}} = 288$ K that interacts with an active fluid inlet temperature of $T_{\text{in}} = 313$ K.

3.2. *FEM Analysis Framework*

To verify that the 1D structural surrogate sizing based on Lamé’s theory remains reliable across the complex 3D topology generated by MOThEA, a rigorous structural validation was performed. The commercial structural suite ANSYS Mechanical was employed to simulate the static load behavior under the maximum design pressure.

Given the ductile nature of high-strength AM steel alloys adopted in advanced manifold manufacturing, the structural integrity was evaluated globally using the von Mises yield criterion. The equivalent von Mises stress (σ_{vm}) was calculated in the solid domain and strictly monitored against the allowable material yield limit:

$$\sigma_{\text{vm}} = \sqrt{\frac{1}{2}\left[(\sigma_1-\sigma_2)^2+(\sigma_2-\sigma_3)^2+(\sigma_3-\sigma_1)^2\right]} \leq \frac{\sigma_{\text{y}}}{SF} \tag{3.4}$$

where $\sigma_1, \sigma_2, \sigma_3$ are the principal stresses, σ_{y} is the material yield strength, and $SF = 1.7$ designates the safety factor. To correctly isolate the linear-elastic response of the material from non-physical localized stress singularities, a specific grid sensitivity analysis was conducted. Three unstructured solid tetrahedral meshes (coarse, $\sim 1.1 \times 10^5$ elements; medium, $\sim 2.2 \times 10^5$ elements; fine, $\sim 5.5 \times 10^5$ elements) were generated. The medium grid was deemed sufficient to capture the stress concentrations around topological junctions without inducing artificial stress divergence.

Regarding the boundary conditions, the worst-case static loading scenario was simulated. A uniform internal static pressure equal to the maximum circuit threshold ($p_{\max} = 240$ bar) was assigned to all internal flow channel faces. Furthermore, to accurately replicate the structural rigid constraints of the real-world installation, *Fixed Support* conditions (zero displacement) were applied to all the primary structural anchoring ports of the hydraulic circuit (refer to the topological mapping in Figure 3.2). Specifically, these rigid constraints were enforced at the functional interfaces bridging the manifold blocks to the filter assembly (port "2" acting as the main outlet of the pre-filter block, and port "1" acting as the main inlet of the post-filter block). Simultaneously, the two primary fluid inlets (ports "8" and "9" on the pre-filter) and the two primary fluid distribution outlets (ports "3" and "4" on the post-filter) were completely constrained. In contrast, the structural boundaries of the functional ports dedicated to hydraulic valves and sensing probes were left free. This constraint configuration allows these terminal connections to undergo unconstrained elastic deformation driven by the internal pressurization, closely replicating their authentic floating boundary behavior within the working machine.

4. RESULTS AND DISCUSSION

As detailed in the numerical setup (Section 3), all full-scale CFD and FEM validations were performed relying on the grid-independent medium computational meshes. The objective of this section is twofold. Firstly, the 3D flow simulations aim to elucidate complex, curvature-induced secondary flow patterns and macroscopic mean-flow separations that cannot be entirely modeled by the 1D analytical surrogate equations, thereby providing a definitive assessment of the actual distributed pressure losses. Secondly, the solid mechanics FEM study serves to verify the global structural integrity of the complex parametrically generated splines, ensuring that no localized stress singularities near the connection ports compromise the structural margins computed by Lamé's sizing framework.

4.1. Surrogate Model Validation & Pressure Losses Reduction

Table 1 summarizes the quantitative performance metrics, comparing the conventional baseline against the MOThEA-optimized geometry in terms of global pressure losses. The topological optimization process yielded a drastic fluid dynamic enhancement: operating under identical boundary conditions, the optimized framework achieved an 84.1% reduction in total pressure drop compared to the traditional drilled manifold.

Table 1: *Quantitative performance comparison among the CFD analysis of the conventional baseline, the CFD validation of the optimized design, and the analytical predictions formulated by the proposed algorithm.*

Configuration Setup	Pressure Losses [bar]	PLs Reduction[1] [%]
Conventional baseline (CFD)	6.42	-
Optimized actual CAD (CFD)	1.02	84.1
Optimized routing (Analytical algorithm)	1.08	83.1

[1] *Compared to the conventional baseline CFD results.*

Interestingly, the pressure drop estimated by the 1D analytical surrogate (1.08 bar) slightly over-predicts the actual CFD result (1.02 bar), with a mismatch of about 6.1%. This conservative bias is the intended consequence of the fully-turbulent worst-case assumption adopted for the friction model (Section 2.2), which upper-bounds the distributed losses over the operating range. Dead-end branches (e.g. pressure probes or closed valve pilot lines, ports "10" and "11") were assigned zero flow, consistent with their role as static terminal stubs; the small localized loss produced in the main channels by the flow passing these dead legs is resolved by the CFD but is not represented in the analytical model. Since this omission acts opposite to the friction over-estimate and is small, the analytical prediction remains a conservative upper bound on the CFD losses. The close agreement between the two values confirms that the analytical surrogate reliably reproduces the pressure drop of the optimized geometry.

To visually elaborate on these numerical achievements, Figure 4.4 maps the velocity magnitude and total pressure streamlines within the pre-filter flow field, directly contrasting the optimized routing against the conventional design. The macroscopic differences dictating the PL drop in the pre-filter block are clearly identifiable. First, the traditional baseline geometry exhibits massive stagnation regions (dead zones) inevitably induced by orthogonal cross-drilling manufacturing. In contrast, MOThEA-generated splines completely bypass these dissipative volumes, maintaining a highly efficient and perfectly attached flow along the entire routing. Secondly, the maximum localized fluid velocity is drastically reduced, dropping from a peak of 24.5 m/s in the baseline to just 12.3 m/s. This is partially attributed to the optimizer autonomously finding a better volumetric trade-off, expanding the internal hydraulic diameter from 31 mm to $\sim$ 38 mm. Lastly, the elimination of sharp 90° junctions suppresses severe *vena contracta* effects, significantly mitigating localized pressure drops. The corresponding total pressure fields (Figure 4.4e-h) confirm the sudden energy dissipation across the sharp corners of the baseline, compared to the smooth pressure gradient of the AM-ready solution.

Similar fluid-dynamic enhancements govern the primary transport channels of the post-filter block, as displayed in Figure 4.5. Although the smooth continuous curvature successfully prevents severe boundary layer separations along the main conduits, localized flow recirculation and large swirling structures are naturally observable within the terminal plenums (Figure 4.5a,b). These macroscopic volumetric expansions are physically required by the functional housing of the hydraulic components (e.g. valves) and cannot be bypassed. Nevertheless, compared to the conventional baseline, the optimized 3D routing ensures that the fluid momentum is delivered to these terminal expansions with minimal intermediate dissipation, confirming the efficiency of the overall structural topology.

4.2. Structural Integrity & Mass Reduction

Alongside the reduction in fluid pressure losses, the topological optimization process produced a significant containment of structural mass. Table 2 details the quantitative mass breakdown, comparing the conventional drilled baseline against the algorithmically generated splines.

Table 2: *Quantitative mass comparison between the conventional baseline manifold block and the MOThEA-optimized free-form topology. The structural assessment assumes AM Inconel 718 (*$\rho_s = 8150$ kg/m^3*).*

Configuration	Pre-Filter [kg]	Post-Filter [kg]	Total Mass [kg]
Conventional baseline	-	-	81.078
Optimized actual CAD	2.598	3.044	5.642
Mass Reduction			**93.1%**

As reported in Table 2, the surrogate-driven algorithm decreased the overall system mass from 81.078 kg to 5.642 kg, corresponding to a relative reduction of 93.1%. This mass saving highlights the potential of free-form topological design for weight-sensitive applications.

To practically realize this geometry and withstand high operational pressures, the selected structural material must exhibit adequate mechanical properties. The analysis relies on Inconel 718 processed via Direct Metal Laser Sintering. This AM material is characterized by an orthotropic yield strength induced by the layer-by-layer manufacturing process: a nominal $\sigma_{y,XY} = 1240$ MPa in the printing plane, and a lower $\sigma_{y,Z} = 1145$ MPa along the vertical build direction. Consequently, the full 3D FEM structural evaluation

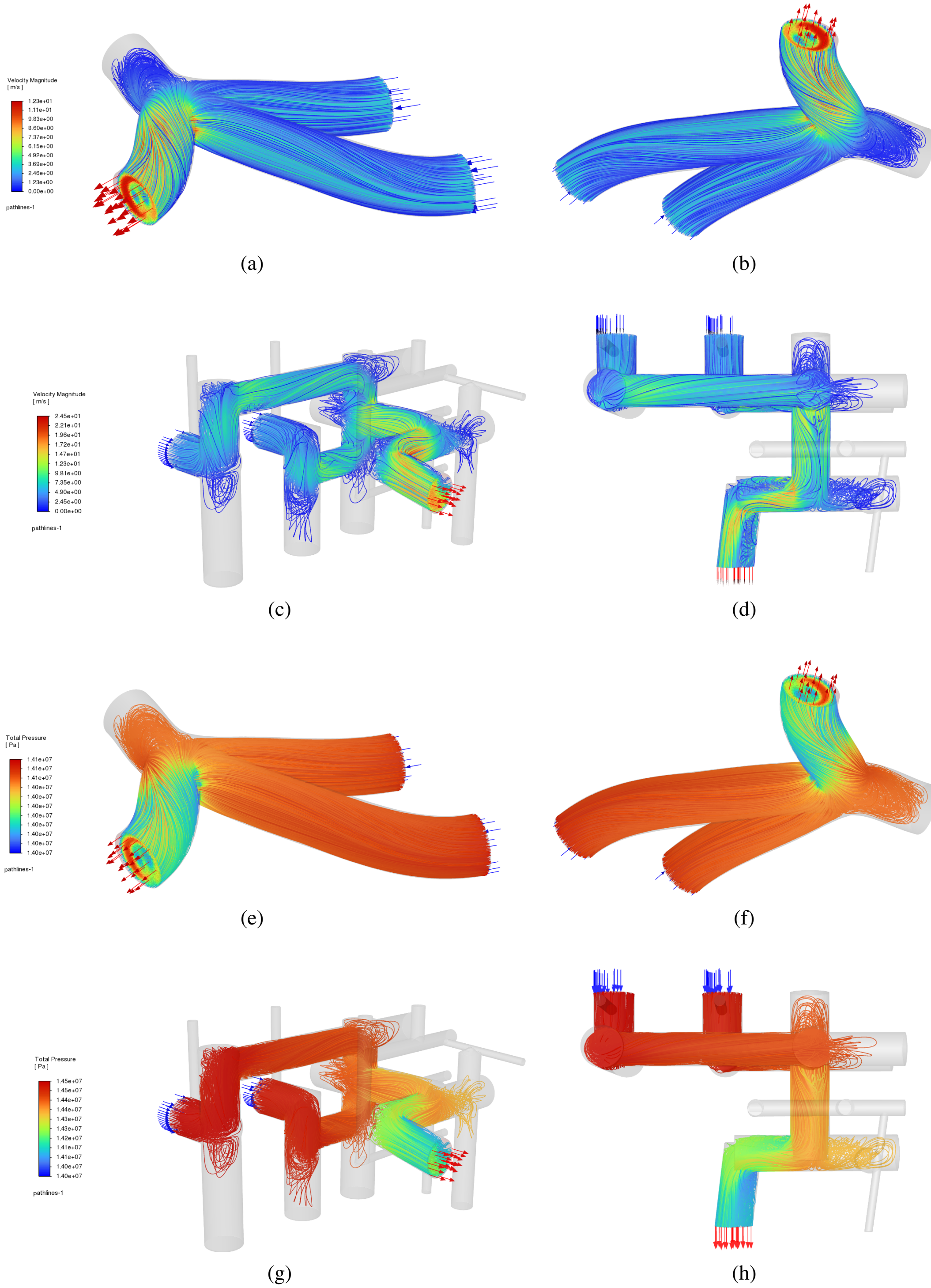

Figure 4.4. *Comparative streamline analysis of the pre-filter domain. Velocity magnitude for the optimized topology (a, b) versus the conventional baseline (c, d). Total pressure distribution for the optimized (e, f) versus the baseline (g, h). Blue and red arrows outside the flow field specify fluid inlets and outlets, respectively. Port "11" is hidden behind the ducts through which fluid flows continuously.*

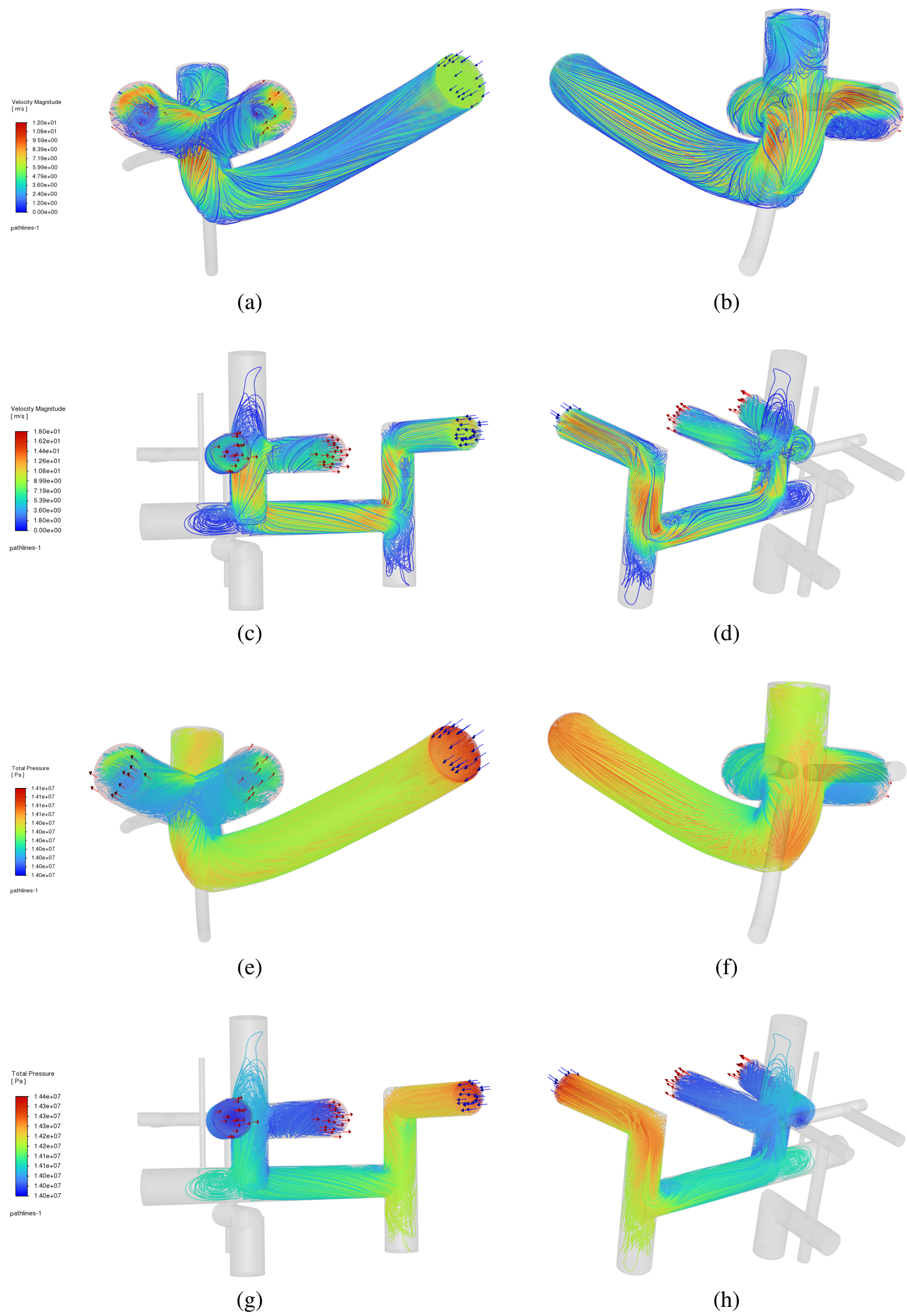

Figure 4.5. *Comparative streamline analysis of the post-filter domain. Velocity magnitude for the optimized topology (a, b) versus the conventional baseline (c, d). Total pressure distribution for the optimized (e, f) versus the baseline (g, h).*

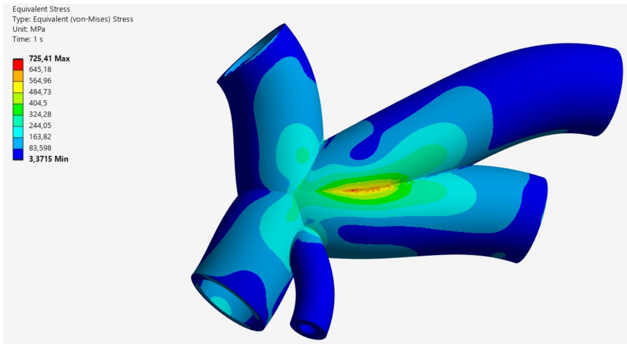

(a)

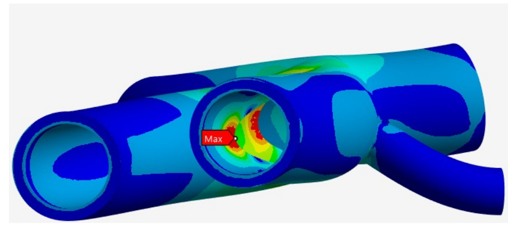

(b)

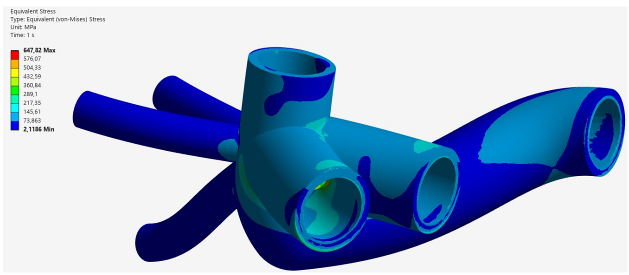

(c)

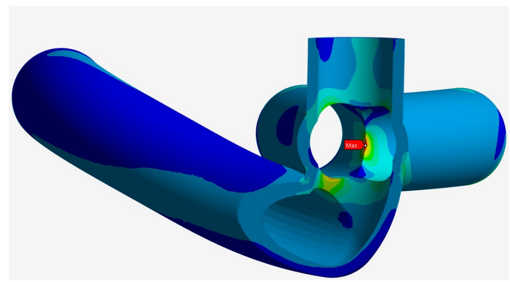

(d)

Figure 4.6. *Analysis of the von Mises equivalent stress (σ_{vm}) distribution. Global structural view of the pre-filter block (a) and a detail on the maximum stress concentration (b). Corresponding global view for the post-filter block (c) and its localized stress peak (d).*

was conducted to verify whether the analytical thickness-sizing equations, based on Lamé's cylinder theory, maintain the stress tensors under maximum pressurization safely below the critical 1145 MPa structural limit. Figure 4.6 presents the resulting von Mises equivalent stress contours for both the optimized pre-filter and post-filter blocks under steady static load conditions. As inherently predicted by the theoretical surrogate model, the vast majority of curvilinear tubular domains exhibits a globally uniform low-magnitude stress field (mainly below 250 MPa, as indicated by the blue contours). This effectively validates Lamé's 1D sizing assumption for the required nominal wall thickness. However, specific nodal stress concentrations naturally arise due to the complex 3D topology and the presence of unavoidable functional geometries. The pre-filter part registers an absolute structural peak of $\sigma_{vm,max} = 725.41$ MPa that occurs at an acute internal saddle point where two fluid branches merge (Figure 4.6b). Similarly, the post-filter region displays a localized equivalent stress peak of 647.82 MPa, positioned exactly at the sharp internal edge of a functional cross-bore that intersects the main housing plenum (Figure 4.6d). These localized peaks and the corresponding safety factors are summarized in Table 3. Even considering these purely localized geometric notch effects under the most critical loading scenario, the maximum recorded effective stress (725.41 MPa) remains strictly contained below the weakest orthotropic yield limit of the AM material. This leads to an intrinsic minimum safety factor of $SF_{min} = 1.58$, driven by the pre-filter saddle-point notch. It is worth noting that this local value is marginally below the nominal design safety factor ($SF = 1.7$) adopted in the 1D Lamé sizing: the analytical thickness rule holds for the bulk tubular walls, while the fully 3D notch at the branch merge locally erodes the margin, without ever reaching yield. This structural margin confirms that the chosen algorithmic layout yields a robust geometry, efficiently decoupling morphological optimization from computationally expensive iterative FEM simulations, and it is precisely why the 3D FEM cross-check complements the 1D surrogate.

Table 3: *Localized von Mises stress peaks and corresponding safety factors for the optimized blocks under the worst-case static load (*$p_{\max} = 240$ bar*). The safety factor is computed against the weakest orthotropic yield limit (*$\sigma_{y,Z} = 1145$ MPa*); the design safety factor used in the 1D sizing is* $SF = 1.7$.

Block	$\sigma_{vm,max}$ [MPa]	$\sigma_{y,Z}$ [MPa]	Safety factor [-]
Pre-filter	725.41	1145	1.58
Post-filter	647.82	1145	1.77

5. CONCLUSIONS

This paper presented a comprehensive full-scale 3D computational validation of MOThEA, a recently developed framework for the automated synthesis of hydraulic manifolds via additive manufacturing. The core strength of the algorithm lies in its reliance on highly efficient analytical surrogate models for both fluid dynamic routing and structural sizing. As demonstrated, this approach completely bypasses the need for computationally prohibitive iterative simulations during the evolutionary loop, allowing the generation of a highly optimized, real-world topology in under 25 minutes on standard desktop hardware.

The full 3D CFD and FEM assessments definitively confirmed the physical reliability and structural viability of the algorithm's assumptions. Operating under severe real-world conditions (maximum flow rate of 400 L/min and internal static pressure of 240 bar), the optimized free-form routing yielded an 84.1% reduction in global pressure drops and a 93.1% decrease in structural mass compared to the conventional cross-drilled baseline. Under these pressure loads, structural integrity was fully guaranteed with a minimum safety factor of $SF_{\min} = 1.58$. While the selected manufacturing material –the Inconel 718 nickel-based super-alloy– entails considerable production costs, its application is fundamentally justified in weight-sensitive sectors, such as aerospace and high-performance mobile machinery, where extreme mass containment translates directly to significant energy and emission savings over the vehicle's life cycle.

Currently, the MOThEA methodology successfully synthesizes the primary fluid dynamic channels and the load-bearing structural envelope. Interfacial valve-spool connections, standardized threaded fixtures, and external mounting brackets are deliberately deferred to a downstream mechanical refinement phase. Accordingly, future research will focus on the complete post-processing of the generated manifolds to conduct rigorous physical test campaigns on 3D-printed prototypes. Furthermore, the mathematical surrogate formulation will be expanded to include thermal gradients and dynamic fatigue stress validations under cyclic hydraulic loading.

References

[1] Beltrami, D., Iora, P., Tribioli, L., Uberti, S.: Electrification of compact off-highway vehicles—overview of the current state of the art and trends. Energies **14**(17) (2021) https://doi.org/10.3390/en14175565

[2] Mahato, A.C., Ghoshal, S.K.: Energy-saving strategies on power hydraulic system: An overview. Proceedings of the Institution of Mechanical Engineers, Part I: Journal of Systems and Control Engineering **235**(2), 147–169 (2021) https://doi.org/10.1177/0959651820931627

[3] Quan, Z., Ge, L., Wei, Z., Li, Y.W., Quan, L.: A survey of powertrain technologies for energy-efficient heavy-duty machinery. Proceedings of the IEEE **109**(3), 279–308 (2021) https://doi.org/10.1109/JPROC.2021.3051555

[4] Li, R., Sun, Q., Ding, X., Zhang, Y., Yuan, W., Wu, T.: Review of flow-matching technology for hydraulic systems. Processes **10**(12) (2022) https://doi.org/10.3390/pr10122482

[5] Du, S., Zhou, J., Hong, J., Zhao, H., Ma, S.: Application and progress of high-efficiency electro-hydrostatic actuator technology with energy recovery: A comprehensive review. Energy Conversion and Management **321**, 119041 (2024) https://doi.org/10.1016/j.enconman.2024.119041

[6] Padovani, D., Dimitriou, P., Minav, T.: Challenges and solutions for designing energy-efficient and low-pollutant machines in off-road hydraulics. Energy Conversion and Management: X **21**, 100526 (2024) https://doi.org/10.1016/j.ecmx.2024.100526

[7] Abe, O., Tsukiji, T., Hara, T., Yasunaga, K.: Flow analysis in pipe of a manifold block. International Journal of Automation Technology **6**, 494–501 (2012)

[8] Zhang, J.J., Wang, J.S., Wang, J.Y., Liu, G., Wang, J.: The optimal design on connection order of network in hydraulic manifold block. In: Advanced Materials Research, vol. 201–203, pp. 2190–2194 (2011). https://doi.org/10.4028/www.scientific.net/AMR.201-203.2190

[9] Alshare, A.A., Calzone, F., Muzzupappa, M.: Hydraulic manifold design via additive manufacturing optimized with cfd and fluid-structure interaction simulations. Rapid Prototyping Journal **25**(9), 1516–1524 (2018) https://doi.org/10.1108/RPJ-03-2018-0064

[10] Hong, Z., Chen-yu, W., Chen-chen, L.: Optimization of flow channel in 3d printing hydraulic manifold block based on response surface method. In: 2019 IEEE 8th International Conference on Fluid Power and Mechatronics (FPM), pp. 217–223 (2019). https://doi.org/10.1109/FPM45753.2019.9035793

[11] Zhu, Y., Wang, S., Zhang, C., Yang, H.: Am-driven design of hydraulic manifolds: Enhancing fluid flow and reducing weight. In: 12th International Fluid Power Conference (12. IFK), Dresden, vol. 1 (2020). https://doi.org/10.25368/2020.23

[12] Rolinck, N., Schmitt, M., Schneck, M., Schlick, G., Schilp, J.: Development workflow for manifolds and fluid components based on laser powder bed fusion. Applied Sciences **11**(16) (2021) https://doi.org/10.3390/app11167335

[13] Chao, Z., Yi, Z., Ruiwen, X., Cong, Z., Huayong, Y., Yi, Z.: Automatic optimisation layout design approach for lightweight and energy-saving additive manufactured hydraulic manifolds. Virtual and Physical Prototyping **19**(1), 2408407 (2024) https://doi.org/10.1080/17452759.2024.2408407

[14] Zhang, C., Zeng, Y., Tang, Y., Gu, Y., Wu, M., Wang, W., Zhu, Y., Bing, X., Yang, H.: Three-dimensional follow-up layout design approach for lightweight hydraulic passage networks. Additive Manufacturing Frontiers (2026) `https://doi.org/10.1016/j.amf.2026.200295`

[15] Itō, H.: Friction factors for turbulent flow in curved pipes. Journal of Basic Engineering **81**(2), 123–132 (1959) `https://doi.org/10.1115/1.4008390`

[16] Swamee, P.K., Jain, A.K.: Explicit equations for pipe-flow problems. Journal of the Hydraulics Division **102**(5), 657–664 (1976) `https://doi.org/10.1061/JYCEAJ.0004542`